



Science Arts & Métiers (SAM)

is an open access repository that collects the work of Arts et Métiers Institute of Technology researchers and makes it freely available over the web where possible.

This is an author-deposited version published in: <https://sam.ensam.eu>
Handle ID: <http://hdl.handle.net/10985/15087>

To cite this version :


Caroline BOLLINGER, Paul RATERRON, Olivier CASTELNAU, Fabrice DETREZ, Sébastien MERKEL - Textures in deforming forsterite aggregates up to 8 GPa and 1673 K - Physics and Chemistry of Minerals - Vol. Volume 43, Issue 6, p.409-417 - 2016

Any correspondence concerning this service should be sent to the repository

Administrator : scienceouverte@ensam.eu



Textures in deforming forsterite aggregates up to 8 GPa and 1673 K

Caroline Bollinger^{1,4} · Paul Raterron¹ · Olivier Castelnau² · Fabrice Detrez^{2,5} · Sébastien Merkel^{1,3} 

Abstract We report results from axisymmetric deformation experiments carried out on forsterite aggregates in the deformation-DIA apparatus, at upper mantle pressures and temperatures (3.1–8.1 GPa, 1373–1673 K). We quantified the resulting lattice preferred orientations (LPO) and compare experimental observations with results from micromechanical modeling (viscoplastic second-order self-consistent model—SO). Up to 6 GPa (~185-km depth in the Earth), we observe a marked LPO consistent with a dominant slip in the (010) plane with one observation of a dominant [100] direction, suggesting that [100](010) slip system was strongly activated. At higher pressures (deeper depth), the LPO becomes less marked and more complex with no evidence of a dominant slip system, which we attribute to the activation of several concurrent slip systems. These results are consistent with the pressure-induced transition in the dominant slip system previously reported for olivine and forsterite. They are also consistent with the decrease in

the seismic anisotropy amplitude observed in the Earth's mantle at depth greater than ~200 km.

Keywords Forsterite · Deformation · High pressure · D-DIA · Lattice preferred orientation · Micromechanical modeling

Introduction

Olivine is the dominant mineral of the Earth's upper mantle (e.g., Frost 2008) and hence controls its mechanical behavior. Mantle deformation translates into lattice preferred orientations (LPO) in rocks which, in turn, induce seismic anisotropy (e.g., Mainprice et al. 2000). In the Earth's upper mantle, anisotropy is regionally dependent (e.g., Gung et al. 2003; Debayle et al. 2005; Yuan and Beghein 2013) but, in average, global average anisotropy is maximum at about 100 km depth. Some studies report a marked decrease at greater depths, with a minimum at 220 km (e.g., Debayle et al. 2005; Yuan and Beghein 2013). Other studies, with other wave types, report a more gradual anisotropy decrease at depth greater than 220 km (e.g., Gung et al. 2003). In the past, this rapid decrease in anisotropy at high depths has been interpreted as a transition from dislocation creep to diffusion creep (e.g., Karato and Wu 1993). Debates emerged in the literature regarding this interpretation, however, with evidences of a pressure-induced transition in olivine dominant slip systems (e.g., Mainprice et al. 2005; Ohuchi et al. 2011) which could explain the seismic observations. Other debates concerns whether mantle olivine LPO could be the result of diffusion creep or dislocation-accommodated grain boundary sliding (Hansen et al. 2012; Miyazaki et al. 2013). Hence, there is a need for a better understanding of the effect of pressure

✉ Sébastien Merkel
sebastien.merkel@univ-lille1.fr

¹ UMET, Unité Matériaux et Transformations, CNRS, INRA, ENSCL, Université de Lille, 59000 Lille, France

² Procédés et Ingénierie en Mécanique et Matériaux (PIMM), CNRS, Arts et Métiers ParisTech, 151, boulevard de l'Hôpital, 75013 Paris, France

³ Institut Universitaire de France, 75005 Paris, France

⁴ Present Address: Bayerisches Geoinstitut (BGI), University of Bayreuth, 95440 Bayreuth, Germany

⁵ Present Address: Laboratoire de Modélisation et Simulation Multi Echelle (MSME), CNRS, Université Paris-Est, Boulevard Descartes, 77454 Marne-la-Vallée Cedex 2, France

(P) and temperature (T) on the deformation-induced LPO in olivine.

The low P (~1.0 GPa), low stress (σ , <300 MPa), high T (~1500 K) deformation of olivine aggregates leads to textures compatible with slip in [100](010) (A-type fabric), which is consistent with extensive data on naturally deformed mantle rocks (Ismail and Mainprice 1998; Tommasi et al. 2000). In parallel, there is a vast literature demonstrating that the addition of water and/or stress can lead to other types of fabrics, compatible with other slip systems (e.g., Jung and Karato 2001; Katayama et al. 2004; Jung et al. 2006). Experiments also indicate a change of olivine and forsterite dominant deformation mechanism with increasing pressure (e.g., Couvy et al. 2004; Mainprice et al. 2005; Durinck et al. 2005; Raterron et al. 2007, 2009, 2011, 2012; Ohuchi et al. 2011; Ohuchi and Irifune 2014). Hence, the olivine fabric diagram obtained at low pressure cannot be easily translated at high pressure.

The effect of hydrostatic pressure on the fabric diagrams of olivine and forsterite, olivine pure Mg-end-member (Fo100), remains to be understood. Ohuchi et al. (2011) report a transition in dry olivine at ~7 GPa from A-type textures toward B-type (induced by [001](010) slip) or C-type (induced by [001](100) slip) textures, in contrast with the study of Jung et al. (2009) who placed such transition at ~3 GPa. Forsterite compression texture at 3.6 GPa and 1573 K does not show such transition (Nishihara et al. 2014). Under wet conditions, a transition to C-type textures is reported for olivine at pressures above ~10 GPa (Ohuchi and Irifune 2014). Such studies, however, present a limited number of points and reported P/T range, with very few data available for pure forsterite. As such, there is a need to clarify the effect of pressure and temperature of deformation textures in forsterite. Here, we use the deformation-DIA apparatus (D-DIA, Durham et al. 2002; Wang et al. 2003) to plastically deform forsterite polycrystals up to 8 GPa and 1673 K and extract the development of LPO in the aggregates as a function of P and T . Experimental textures are then compared with results of the visco-plastic second-order self-consistent model (SO, Ponte Castañeda 2002; Detrez et al. 2015) in order to estimate the dominant slip systems in each condition.

Methods

Sample preparation and D-DIA experiment

Deformation experiments were performed in the D-DIA apparatus at the X17B2 beamline of the National Synchrotron Light Source (Upton, NY, USA). In this study, we plastically deformed polycrystals of forsterite at pressures ranging from 3.1 to 8.1 GPa and temperature between 1373

and 1673 K at constant uniaxial strain rates in the range -2.4×10^{-5} to $5.5 \times 10^{-5} \text{ s}^{-1}$ (Table 1).

The forsterite starting material was prepared by crushing one gem quality single crystal in an alumina-mortar, grinding it to a fine-grained powder at the optical scale (average grain size 10 μm). The starting crystal was synthesized at room pressure by the Czochralski (CZ) process (e.g., Takei and Kobayashi 1974). It was dry, i.e., no hydroxyls were detectable using Fourier's transform infrared spectroscopy (FTIR, see Raterron et al. 2007). FTIR measurements after the runs show that most of the samples contain more than 200 ppm H/Si, according to the Paterson calibration (Paterson 1982).

Specimens were loaded into the D-DIA deformation cell in between two machinable alumina end plugs, which become hard pistons at run conditions. Two types of experiments were performed. Runs #65, #68, #69, #70 were carried out with one sample of pure forsterite powder in the compression column. Runs #80, #81, #82, #87, #88, #89 and #90 were performed with two powder samples, one of pure forsterite and one of San Carlos olivine atop one another, separated by a thin layer of alumina sandwiched in between Re foils. Both forsterite and olivine powders were mixed with a small fraction (5 wt%) of natural enstatite ($\text{En}_{84}\text{Fs}_{13}\text{Wo}_3$) powder, in order to buffer the orthopyroxenes (Opx) activity ($a_{\text{Opx}} = 1$) and limit grain growth during the runs (McDonnell et al. 2000).

More details about samples, experiments and rheology analysis are available in previous papers (Bollinger et al. 2012, 2014, 2015). Here, we present the final analysis of the dataset, focusing on LPO development in the forsterite aggregates.

Deformation protocol

A total of 13 D-DIA experiments were performed, resulting in 26 steady-state deformation conditions in axial compression (see Bollinger et al. 2014, 2015). Most experiments were performed following the same protocol. The cell is first pressurized at room T and then brought to high T by supplying power to the graphite heater. Hydrostatic conditions are maintained at high T for 1 h at the onset of the run. This ensures the sintering of pistons and specimens, and the restoration of specimen damages as well as the relaxation of internal stress resulting from cold compression.

Axisymmetric deformation of the cell assembly is initiated by displacing the vertical D-DIA anvils at a fixed rate until the desired sample strain (typically several %, see Fig. 1) at constant strain rate is achieved. Several temperature and/or sample strain-rate conditions are usually tested during each run (Table 1). At the end of the run, T is quenched by turning off the power supply and both D-DIA vertical anvils are stopped. P is then decreased gradually to room- P for 1 to 2 h.

Table 1 Run numbers, conditions of deformation (geometry, temperature, pressure, differential stress, and strain rate), total strain applied in each deformation step, [OH] content measured in the sample after the experiment, and texture observations for all available datasets

Run #	Deformation	<i>T</i> (K)	<i>P</i> (GPa)	σ (MPa)	$\dot{\epsilon}$ (10^{-5} s^{-1})	Strain in step (%)	Paterson (1982) (ppm H/Si)	Bell et al. (2003) (ppm H/Si)	Comparison with models
65	Axial	1373	5.8 (0.2)	1196 (115)	3.8 (0.07)	23	531	1224	(010) Dominant
65	Lateral	1373	5.2 (0.2)	−637 (210)	−2.4 (0.05)	−7			Direction [100] dominant
65	Axial	1373	5.6 (0.2)	1242 (123)	5.5 (0.06)	9			(010) Dominant
68	Axial	1373	4.1 (0.1)	489 (122)	4.8 (0.05)	33	–	–	(010) Dominant
69	Axial	1373	5.6 (0.1)	263 (48)	4.4 (0.06)	18	–	–	(010) Dominant
70	Axial	1373	3.1 (0.1)	959 (56)	4.5 (0.17)	42	175	375	(010) Dominant
79	Axial	1473	3.1 (0.1)	146 (96)	1.7 (0.35)	6	–	–	Weak (010)
80	Axial	1473	3.8 (0.1)	262 (194)	1.5 (0.17)	12	–	–	(010) Dominant
81	Axial	1373	5.6 (0.2)	382 (315)	2.3 (0.20)	5	1777	3769	Not measured
81	Axial	1373	4.6 (0.2)	493 (228)	2.2 (0.03)	6			(010) Dominant
81	Axial	1573	4.8 (0.1)	78 (181)	2.7 (0.05)	9			(010) Dominant
81	Axial	1573	4.9 (0.2)	341 (88)	4.5 (0.20)	11			(010) Dominant
82	Axial	1373	7.8 (0.2)	831 (337)	0.9 (0.05)	6	–	–	Undefined
82	Axial	1573	7.1 (0.1)	163 (83)	1.7 (0.01)	9			(010) Dominant
87	Axial	1373	5.1 (0.4)	737 (117)	1.9 (0.06)	10	–	–	(010) Dominant
87	Axial	1573	4.6 (0.4)	203 (241)	4.4 (0.16)	15			(010) Dominant
87	Axial	1573	6.0 (0.2)	276 (251)	3.4 (0.38)	19			(010) Dominant
88	Axial	1473	7.0 (0.4)	884 (110)	0.9 (0.05)	8	493	1371	(001) Dominant
88	Axial	1673	7.6 (0.3)	272 (256)	2.0 (0.43)	4			Undefined
89	Axial	1473	5.5 (0.4)	535 (244)	1.1 (0.03)	4	110	493	(100) Dominant
89	Axial	1473	5.6 (0.4)	504 (217)	0.5 (0.40)	5			Undefined
89	Axial	1673	5.0 (0.2)	83 (62)	1.2 (0.20)	6			Undefined
89	Axial	1673	4.5 (0.8)	248 (242)	2.2 (0.40)	5			Undefined
90	Axial	1473	7.1 (0.4)	796 (291)	2.7 (0.02)	9	1565	3327	(100) Dominant
90	Axial	1673	8.1 (0.4)	118 (154)	4.5 (0.01)	12			Undefined

Texture observations for lateral compression in run 65 allows for determining a dominant slip direction. Other deformation steps are performed in axial compression and allow for the determination of a dominant slip plane. Stresses and strains are set positive for case of axial compression

Most deformation experiments were performed in axial compression, by advancing the vertical anvils and reducing the sample length. One test during runs #65 was performed in lateral compression, by retracting the vertical anvils and extending the sample length. In axial compression, the sample volume is kept constant while shortening the sample. It is hence analogous to a “compression” experiment performed under ambient pressure. In lateral compression, the sample volume is kept constant while lengthening the sample. It is hence analogous to a “tension” experiment performed under ambient pressure. From a mechanical point of view, however, the sample is being submitted to stress by the lateral anvils, hence the term “lateral compression.”

X-ray measurements and LPO analysis

Taking advantage of the ten-element energy-dispersive multi-detector of the X17B2 beamline (Weidner et al.

2010), *P* and σ are measured in situ following the protocol described by Bollinger et al. (2012). Specimen strain (ϵ) and strain rate ($\dot{\epsilon}$) are measured by time-resolved X-ray radiography (Vaughan et al. 2000) from the positions on radiographs of the metal foils placed at sample ends.

Sample LPO is measured in situ using the variation of diffraction peak intensities with orientation, as first described in Bollinger et al. (2012). For forsterite, we used, when possible, the first-order diffraction lines: 021, 101, 002, 130, 131, 112, 041, 210. As in Bollinger et al. (2012), the Polydefx software (Merkel and Hilairat 2015) was used to correct the raw data for detector sensitivity and shadow effect from the D-DIA. The experimental LPO were then exported for further processing in Beartex (Wenk et al. 1998) and extract the corresponding orientation distribution function (ODF), assuming axial symmetry around the deformation axis. Textures are then represented with inverse pole figures (IPF, Fig. 1). For axial compression

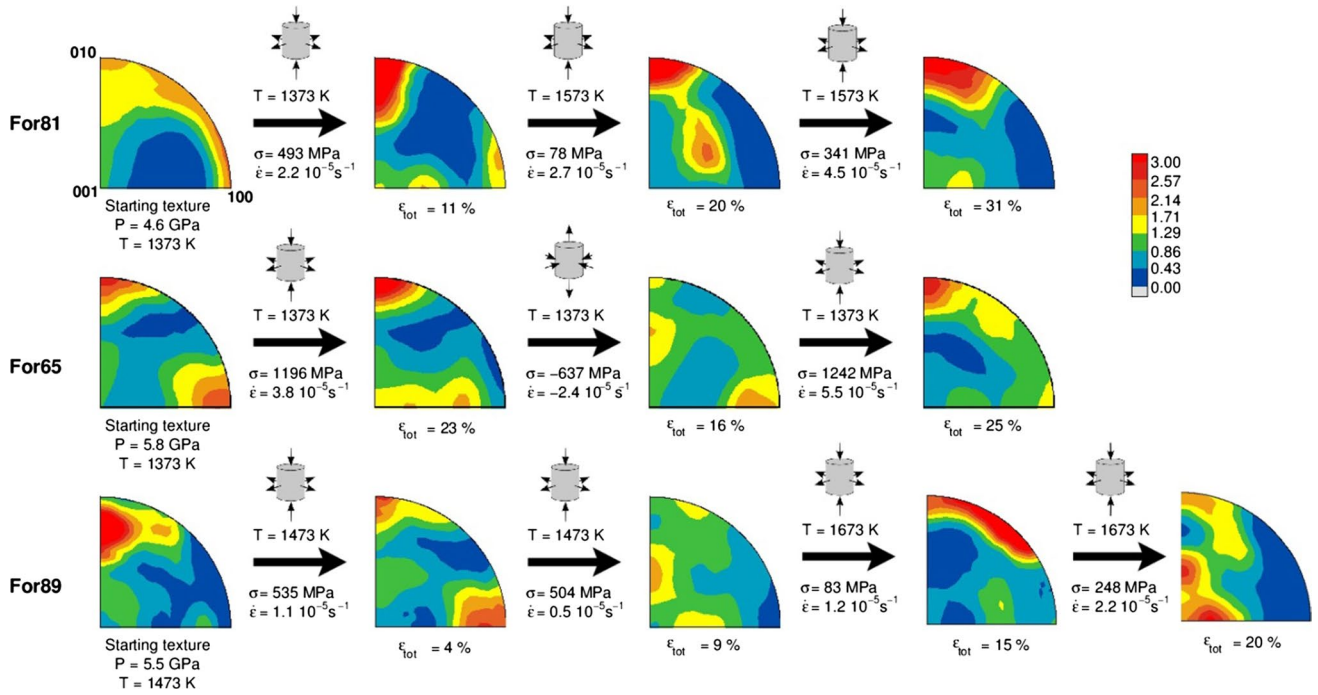


Fig. 1 Typical textures obtained in experiments. Inverse pole figures of the compression direction for axial compression experiments. Inverse pole figure of the lengthening direction for lateral compression experiment. Equal area projections. Linear scale in multiples of

a random distribution. Experimental pressures (P), temperatures (T), stresses (σ), total strains (ϵ) and strain rates ($\dot{\epsilon}$) are indicated on the figure

experiments, we use inverse pole figures of the compression direction. For lateral compression experiments, we use inverse pole figures of the lengthening direction.

Electron backscattered diffraction (EBSD) is a method of choice for the study of LPO under ambient conditions. The LPO extracted from X-ray diffraction at the X17B2 beamline were validated with post-mortem EBSD measurements on run #65 (Bollinger et al. 2012). The current study focuses on LPO measured in situ, using X-ray diffraction. While further EBSD measurements could have been useful for a full understanding of the mechanisms involved, they are no more possible on the current samples as most of them have been used for FTIR and TEM analyses.

Grain growth

The forsterite powder was mixed with 5 wt% enstatite to limit grain growth. At 1673 K, however, we observed large changes in relative diffraction intensities between each deformation step. This is an indication of fast recrystallization of the sample (e.g., Figure 3 in Hilairet et al. 2012). Recrystallization implies grain growth and a fast reorientation of sample grains. Under such conditions, the number of grains probed by the X-ray beam is changing, can be insufficient, and the extracted LPO become variable. Such behavior can be difficult to observe in polychromatic

diffraction with point detectors, but is clearly visible in the monochromatic diffraction images of Hilairet et al. (2012). Hence, in this paper, fabrics measured at 1673 K will be labeled as “undefined,” as they evolve with time, with no clear connection between the direction of deformation and the extracted LPO.

Micromechanical model

In deformation experiments performed in shear, and especially for orthorhombic crystals such as forsterite, sample LPO are often directly associated with a dominant slip system by identifying the slip direction to the maximum orientation concentration close to the direction of shear and the slip plane to the maximum orientation concentration normal to the shear plane. Such direct association between texture type and slip system is more difficult for slip systems with multiple symmetry equivalents (e.g., $[001]\{110\}$), if multiple systems are active, or for textures obtained in compression.

Hence, in order to help with the data interpretation, we perform polycrystal plasticity simulations of the expected fabrics using the second-order (SO) self-consistent model, initially proposed by Ponte Castañeda (2002) and extended by Detrez et al. (2015). This mean-field micromechanical model accounts for the slip systems at the grain level and

Table 2 CRSS and simulated slip system activities in SO calculations

Dominant slip system	CRSS and activity						
	[100](010)	[001](010)	[001](100)	[100]{021}	[100](001)	[001]{110}	Isotropic
[100](010)	10 24–22 %	50 3–2 %	50 2–2 %	50 2–2 %	50 2–2 %	50 3–4 %	50 66–66 %
[001](010)	50 3–2 %	10 24–22 %	50 1–2 %	50 4–3 %	50 1–2 %	50 2–3 %	50 65–65 %
[001](100)	50 3–2 %	50 2–3 %	10 21–23 %	50 3–2 %	50 1–1 %	50 2–2 %	50 68–68 %
[100]{021}	50 0–0 %	50 3–1 %	50 1–1 %	10 33–38 %	50 1–1 %	50 2–1 %	50 61–58 %
[100](001)	50 2–3 %	50 3–2 %	50 1–1 %	50 2–3 %	10 22–23 %	50 2–1 %	50 69–68 %
[001]{110}	50 3–1 %	50 1–2 %	50 0–0 %	50 3–2 %	50 0–0 %	10 30–34 %	50 62–60 %
[001](100)	50	50	10	50	10	50	50
[100](001)	2–2 %	2–2 %	14–14 %	2–2 %	14–14 %	2–2 %	64–64 %

Each line is a simulation with a different dominant slip system. For each simulation, we report the CRSS of each slip system (top number), their plastic relative activities in axial compression (first percentage) and lateral compression (second percentage)

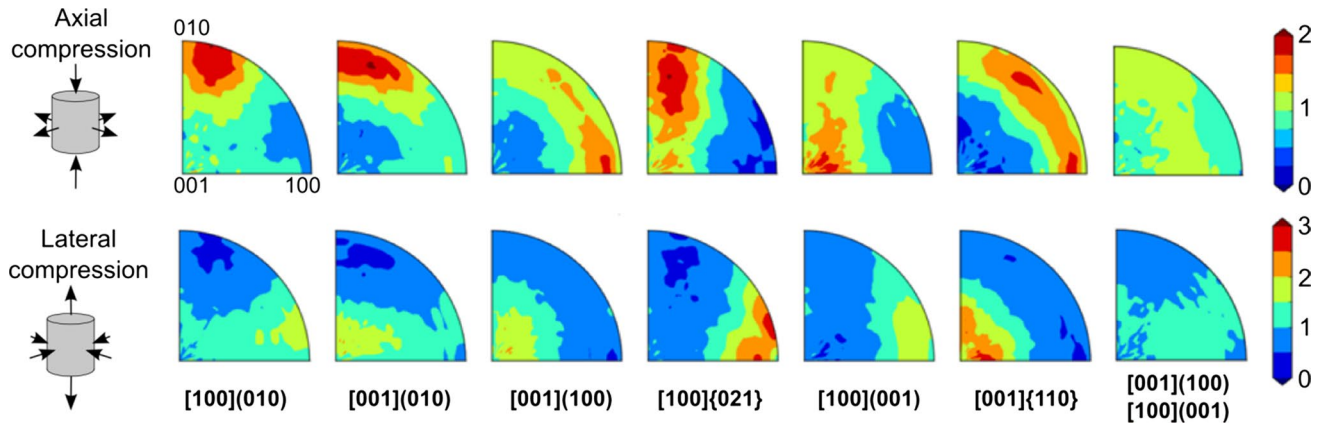


Fig. 2 Inverse pole figure representing the simulated LPO for a forsterite aggregate deformed in axial (*top row*) and lateral (*bottom row*) compression using the parameters of the Table 2. Equal area projections. Linear scale in multiples of a random distribution. For axial

compression: inverse pole figure of the compression direction. For lateral compression: inverse pole figure of the lengthening direction. The dominant slip system is indicated below the figure

an isotropic relaxation mechanism. Olivine is lacking four independent slip systems at the grain level, which is necessary to accommodate any arbitrary plastic deformation in the aggregate. Hence, an additional relaxation mechanism is required. The microscopic origin of the relaxation is not known. It could relate to grain boundary sliding, dynamic recrystallization, diffusion, or disclinations.

We define seven plastic models allowing for different dominant slip systems (Table 2). For each, we arbitrarily set the strength of the dominant deformation mechanism to 10 and to 50 for all others. Simulations are performed for a 1000 grains random starting aggregate, and we calculate the polycrystal LPO after 50 % deformation in axial (final state

$\varepsilon_{xx} = \varepsilon_{yy} = 0.25$ and $\varepsilon_{zz} = -0.5$, where z is the compression direction) and lateral (final state $\varepsilon_{xx} = \varepsilon_{yy} = -0.25$ and $\varepsilon_{zz} = 0.5$) compression (Fig. 2). In all cases, the isotropic mechanism accommodates between 55 and 70 % of the plastic strain, while the enforced dominant slip system accommodates between 20 and 40 % of the deformation (Table 2).

The isotropic mechanism allows removing the fictitious $\langle 1\bar{1}0 \rangle \{111\}$ slip system used in previous computations (e.g., Tommasi et al. 2000; Castelnau et al. 2009, 2010). Because of the strong plastic anisotropy in olivine, the isotropic mechanism accommodates a significant portion of the strain, even if its strength is set to a large value (Detrez

et al. 2015). It should be noted, however, that the activity of the isotropic mechanism does not change the locations of the minima and maxima in the simulated textures, but only their intensity. Changing the strength of this mechanism will not change the interpretation of textures in terms of a dominant slip system in an experiment.

Results

Micromechanical modeling

Figure 2 presents the calculated fabrics for each plastic model of Table 2. In axial compression (sample shortening), deformation involving (100), (010), and (001) as dominant slip plane lead to maxima at 100, 010, and 001 in the inverse pole figures, respectively. If dominant, those slip planes can hence be easily deduced from compression textures. Systems involving {110} or {021} lead to broader maxima and will hence be more difficult to identify. The joint activation of multiple dominant slip systems (such as [100](001) and [001](100) together) leads to a nearly random LPO, with no marked intensity, in which the dominant slip plane can be difficult to identify.

Simulations in lateral compression (sample lengthening) lead to an interesting result: a dominant [100] or [001] slip directions induces a maximum at 100 and 001, respectively. Contrary to common belief, it is hence possible to deduce a dominant glide direction from axial deformation experiments, as long as the interpretation of experimental textures is validated with micromechanical models. Dominant [100] slip direction in olivine will lead to a maximum at 100 in the inverse pole figure of the lengthening direction for lateral compression. Reversely, dominant [001] slip direction will lead to a maximum at 001. Lateral compression is hence an effective method for identifying the dominant glide direction in olivine.

Experimental textures

Representative fabrics measured in forsterite are presented in Fig. 1. This paragraph will describe the orientation relation between the different crystallographic axes and a specific sample direction: the shortening direction for the axial compression data, and the lengthening direction for the lateral compression data. All other results are listed in Table 1.

In run #81, the sample displays relatively weak LPO at the beginning of the run, with a maximum intensity spreading from the 010 to the 100 pole. After a step in axial compression at 4.6 GPa and 1373 K, the sample develops a LPO with a clear maximum intensity at the 010 pole. The sample is then further deformed at higher temperature (1573 K).

The maximum at 010 becomes stronger and minima appear between 100 and 011. These observations indicate a dominant (010) glide plane at 4.6 GPa and 1373–1573 K.

Run #65 is a cycle of axial compression (sample shortening), followed by lateral compression (sample lengthening), and again axial compression at ~5.8 GPa and 1373 K. After the first compression, the sample texture is characterized by a sharp maximum at 010. The following lateral compression induces a weaker texture, with a maximum intensity at 100. Finally, the last axial compression cycle induces, again, a sharp maximum at 010, as in the first deformation step. Those observations are consistent with the activation of the dominant slip in the [100] direction and in the (010) plane at ~5.8 GPa and 1373 K.

In run #89, first performed at 5.5 GPa and 1473 K, the sample starts from an initial LPO with a maximum intensity close to 010. After the two first deformation steps in axial compression, one can observe two maxima at 010 and 100, with a weaker LPO. Hence (010) is not a single dominant slip plane in this run. The somewhat weak final textures do not allow for extracting information for a dominant slip plane under these conditions. Temperature is then increased to 1673 K. Compression textures are strong at a strain of 15 %, with a maximum between 010 and 110. However, further compression to a strain of 20 % under similar conditions leads to a maximum at 001, inconsistent with the previous measurement. As reported by Hilairet et al. (2012), diffraction intensity variations with orientations change rapidly above 1600 K, because of fast grain growth and/or recrystallization. Dominant deformation mechanisms are hence difficult to extract from X-ray diffraction textures. Further analysis with EBSD could have helped with the interpretation of the high temperature textures that cannot be evaluated with X-rays, but they were not possible with the current sample.

Effect of P and T on forsterite compression textures

Information on slip systems deduced from the experimental textures is summarized in Fig. 3a. At 1373 K, we observe textures compatible with a dominant (010) slip plane up to 6 GPa, whatever the water content. At 8 GPa, texture is weak with no clear connection to a dominant slip plane. At 1473 K, the (010) slip plane is dominant at ~4 GPa. Results are inconsistent above 4 GPa, with different experiments leading to different results. At 1573 K, we observe textures consistent with (010) as a dominant slip plane up ~7 GPa, with no measurements at higher pressure. At 1673 K, in the whole tested pressure range, no clear texture can be defined, neither in dry (<200 ppm H/Si, see Kohlstedt et al. 1996) nor wet (>200 ppm H/Si) conditions. Grain growth and/or recrystallization do not allow the measurement of consistent textures with the capabilities of the present setup

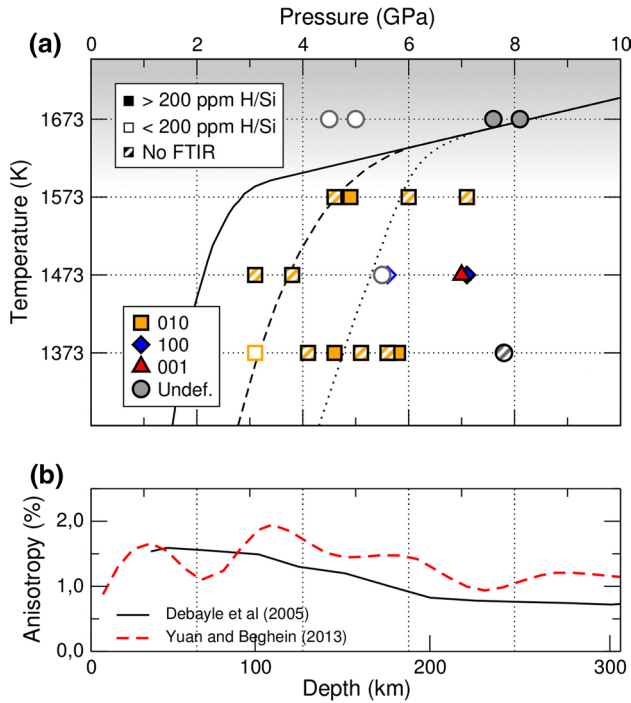


Fig. 3 **a** Dominant glide planes deduced as a function of the pressure and temperature. *Orange square* dominant slip in (010), *blue diamond* dominant slip in (100), *red triangle* dominant slip in (001), *gray circle* weak or inconsistent texture. *Lines* are indicating three typical geotherms (*dashed line* oceanic geotherm, 20 Ma, *dotted line* oceanic geotherm, 80 Ma, *solid line* continental geotherm). *Gray shading* above ~1600 K indicates temperatures where grain growth and/or recrystallization do not allow the measurement of consistent textures with the capabilities of the present setup. *Filled symbols* samples with high water content. *Open symbols* sample with low water content. *Crossed symbols* sample with no water content measurement. **b** Average amplitude of azimuthal anisotropy (dependence of seismic wave-speed within a horizontal layer) for vertically polarized shear-waves observed as a function of depth in the Earth's mantle (Debayle et al. 2005; Yuan and Beghein 2013)

at this high P , T . This last observation is consistent with TEM observations of evidences of recovery at temperatures above 1600 K (Bollinger et al. 2015). As shown in Fig. 3 and Table 1, there is no clear connection between the observed textures and sample water content or stress level.

Discussion

Effect of P and T on forsterite plasticity

At pressure and temperature lower than 6 GPa and 1600 K, we observe consistent LPO, compatible with dominant slip on (010) plane, with a clear determination of a dominant [100](010) slip system in run #65 at 4.6 GPa and 1373 K. Above 6 GPa, we suspect the activation of multiple dominant slip systems, leading to a weaker LPO that is difficult

to measure with the current setup. The change in observed textures above 6 GPa may be related to the transition of deformation mechanism expected at these conditions (e.g., Couvy et al. 2004; Durinck et al. 2005, 2007; Raterron et al. 2007, 2009, 2011, 2012; Jung et al. 2009) or a transition to a regime dominated by diffusion. Indeed, Nishihara et al. (2014) have shown that both diffusion and dislocation creep play an important role in the rheology of forsterite aggregates. The present data, however, do not allow drawing a final conclusion on the topic.

LPO developed in olivine are usually interpreted as a result from the activation of a single dominant (or major) slip system. Below 6 GPa and 1600 K, our data are consistent with this observation with textures indicating a clear dominant (010) slip plane. Above 6 GPa and 1600 K, forsterite plasticity seems governed by several concurrent mechanisms.

Although the water content was not controlled during our experiments, FTIR analyses show that the deformation occurred in “wet” conditions (details in Bollinger et al. 2015) with more than 200 ppm H/Si for most of the forsterite samples. Our observations at 1373 K and 4.6 GPa indicate a dominant [100](010) slip system, consistent with a A-type LPO (Jung et al. 2006). C-type or E-type LPOs with a dominant (100) or (001) slip plane are expected for wet olivine but do not clearly appear in our experiments (Table 1; Fig. 3). Hence, water content did not significantly affect our measured fabrics. Ohuchi et al. (2011) described the pressure effect on the LPO in “dry” olivine aggregates in shear and showed a transition from A-type LPO to B-type or C-type about 7.6 GPa. In a later publication (Ohuchi and Irifune 2014), they placed such transition at ~10 GPa for water-saturated olivine. Our data in Fig. 1 indicate a transition from a 010 compression LPO to a different LPO above 6 GPa. This transition, observed in relatively wet forsterite, is hence at a P about 1.5 GPa lower than that of Ohuchi et al. (2011) in “dry” olivine. Difference in sample composition and water content may explain this small pressure difference.

Implications for upper mantle anisotropy

In the Earth's upper mantle, seismic anisotropy is maximum at about 100 km depth, where $P = 3.2$ GPa (Fig. 3b). According to Yuan and Behein (2013), it decreases markedly at lower depths with a minimum located at 220 km ($P = 7.1$ GPa) and increases again to a secondary maximum at ~300 km ($P = 9.8$ GPa).

Our data on forsterite indicate a dominance of slip in (010) up to ~6 GPa, with a transition in compression textures occurring at higher pressures. Interestingly, the pressures at which our experimental LPO become complex, with uncertainties regarding the dominant slip system, do

correspond to depths with a minimum in seismic anisotropy. Hence we can speculate that the minimum of global anisotropy observed at 220 km depth is related to a change of plastic mechanism in olivine.

The experimental setup used here did not allow experiments at higher pressure. Hence, our data do not allow determining the dominant slip system at lower depths. Texture measurements by Ohuchi et al. (2011) and Ohuchi and Irifune (2014), however, lead to a dominant [001](100) or [001](hk0) at $P \sim 7\text{--}11$ GPa in wet and dry olivine, in agreement with the TEM work of Couvy et al. (2004), the single crystal experiments of Raterron et al. (2007, 2009, 2011, 2012), and predictions based on numerical modeling of Durinck et al. (2005).

Hence, we can speculate the following scenario for olivine fabrics in the Earth's mantle. Above 200 km, olivine plasticity leads to fabrics consistent with a dominant [100](010) slip. At ~ 220 km depth, a transition occurs in olivine plasticity, leading to inconsistent textures and a weak seismic anisotropy. As pressure increases, textures become consistent with slip along [001] in planes such as (100), (010) or (hk0) thus explaining the increasing observed anisotropy down to 300 km.

Conclusion

Steady-state deformation experiments were performed on forsterite aggregates in the D-DIA coupled with synchrotron radiation on polycrystalline forsterite at P – T conditions representative of upper mantle geotherms down to depths of ~ 250 km (P , T range from 3.1 to 8.1 GPa and from 1373 to 1673 K, respectively). The obtained fabrics are then compared with results of micromechanical models for the extraction of dominant plastic mechanism in the forsterite aggregate.

Below 6 GPa and 1600 K, we observe consistent LPO, compatible with dominant slip on (010), with a clear determination of a dominant [100](010) slip system at 4.6 GPa and 1373 K. Above 6 GPa, we suspect the activation of multiple dominant slip systems, leading to a weaker LPO that is difficult to measure with the current setup.

In the Earth's mantle, we hence speculate that above 200 km depths, olivine fabrics are controlled by a mechanism consistent with slip along [100](010). The seismic anisotropy minimum observed at 220 km is connected to a change of dominant deformation mechanism in olivine, leading to weaker or inconsistent fabric. Deeper in the mantle, olivine plasticity becomes more consistent and, hence, allows for the development of further seismic anisotropy.

Acknowledgments The authors thank Hayian Chen (Stony Brook University), Jennifer Girard (Florida International University, now at Yale University) and Caleb Holyoke (Texas A&M University, now at the University of Akron), for their assistance at the NSLS X17B2 beamline, K. Yuan (Univ. California Berkeley) for assistance in the anisotropy plot of Fig. 3b, N. Hilaiet for useful discussions and the two anonymous reviewers for their comments. This research was supported by the Consortium for Materials Properties Research in Earth Sciences (COMPRES) under NSF Cooperative Agreement EAR 06-49658, as well as the Agence Nationale de la Recherche (ANR) Grant BLAN08-2_343541 “Mantle Rheology.” Use of the National Synchrotron Light Source, Brookhaven National Laboratory, was supported by the U.S. Department of Energy, Office of Science, Office of Basic Energy Sciences, under Contract No. DE-AC02-98CH10886.

References

- Bollinger C, Merkel S, Raterron P (2012) In situ quantitative analysis of stress and texture development in forsterite aggregates deformed at 6 GPa and 1373 K. *J Appl Crystallogr* 45:263–271
- Bollinger C, Raterron P, Cordier P, Merkel S (2014) Polycrystalline olivine rheology in dislocation creep: revisiting experimental data to 8.1 GPa. *Phys Earth Planet Inter* 228:211–219
- Bollinger C, Merkel S, Cordier P, Raterron P (2015) Deformation of forsterite polycrystals at mantle pressure: comparison with Fe-bearing olivine and the effect of iron on its plasticity. *Phys Earth and Planet Inter* 240:95–104
- Castelnau O, Blackman DK, Becker TW (2009) Numerical simulations of texture development and associated rheological anisotropy in regions of complex mantle flow. *Geophys Res Lett* 36:L12304
- Castelnau O, Cordier P, Lebensohn RA, Merkel S, Raterron P (2010) Microstructures and rheology of the Earth's upper mantle inferred from a multiscale approach. *C R Phys* 11:304–315
- Couvy H, Frost DJ, Heidelbach F, Nyilas K, Ungár T, Mackwell S, Cordier P (2004) Shear deformation experiments of forsterite at 11 GPa—1400°C in the multianvil apparatus. *Eur J Mineral* 16:877–889
- Debaille E, Kennett B, Priestley K (2005) Global azimuthal seismic anisotropy and the unique plate-motion deformation of Australia. *Nature* 433:509–512
- Detrez F, Castelnau O, Cordier P, Merkel S, Raterron P (2015) Effective viscoplastic behavior of polycrystalline aggregates lacking four independent slip systems inferred from homogenization methods; application to olivine. *J Mech Phys Solids* 83:199–220
- Durham WB, Weidner DJ, Karato S-I, Wang Y (2002) New developments in deformation experiments at high pressure. *Rev Mineral Geochem* 51:21–49
- Durinck J, Legris A, Cordier P (2005) Pressure sensitivity of olivine slip systems: first-principle calculations of generalised stacking faults. *Phys Chem Miner* 32:646–654
- Durinck J, Devincere B, Kubin L, Cordier P (2007) Modeling the plastic deformation of olivine by dislocation dynamics simulations. *Am Mineral* 92:1346–1357
- Frost DJ (2008) The upper mantle and transition zone. *Elements* 4:171–176
- Gung Y, Panning M, Romanowicz B (2003) Global anisotropy and the thickness of continents. *Nature* 422:707–711
- Hansen LN, Zimmerman ME, Kohlstedt DL (2012) Laboratory measurements of the viscous anisotropy of olivine aggregates. *Nature* 492:415–418
- Hilaiet N, Wang Y, Sanehira T, Merkel S, Mei S (2012) Deformation of olivine under mantle conditions: an in situ high-pressure,

- high-temperature study using monochromatic synchrotron radiation. *J Geophys Res Solid Earth* 117:B01203
- Ismail WB, Mainprice D (1998) An olivine fabric database: an overview of upper mantle fabrics and seismic anisotropy. *Tectonophysics* 29:145–157
- Jung H, Karato S-I (2001) Water-induced fabric transitions in olivine. *Science* 293:1460–1463
- Jung H, Katayama I, Jiang Z, Hiraga T, Karato S-I (2006) Effect of water and stress on the lattice-preferred orientation of olivine. *Tectonophysics* 421:1–22
- Jung H, Mo W, Green HW (2009) Upper mantle seismic anisotropy resulting from pressure-induced slip transition in olivine. *Nat Geosci* 2:73–77
- Karato S-I, Wu P (1993) Rheology of the upper mantle: a synthesis. *Science* 260:771–778
- Katayama I, Jung H, Karato S-I (2004) New type of olivine fabric from deformation experiments at modest water content and low stress. *Geology* 32:1045
- Kohlstedt DL, Keppeler H, Rubie DC (1996) Solubility of water in the α , β and γ phases of $(\text{Mg, Fe})_2\text{SiO}_4$. *Contrib Mineral Petrol* 123:345–357
- Mainprice D, Barruol G, Ismail WB (2000) The seismic anisotropy of the Earth's mantle: from single crystal to polycrystal. In: Karato S, Forte A, Liebermann R, Masters G, Stixrude L (eds) *Earth's deep interior: mineral physics and tomography from the atomic to the global scale*. AGU, Washington, DC, pp 237–262
- Mainprice D, Tommasi A, Couvy H, Cordier P, Frost DJ (2005) Pressure sensitivity of olivine slip systems and seismic anisotropy of Earth's upper mantle. *Nature* 433:731–733
- McDonnell RD, Peach CJ, van Roermund HLM, Spiers CJ (2000) Effect of varying enstatite content on the deformation behavior of fine-grained synthetic peridotite under wet conditions. *J Geophys Res Solid Earth* 105:13535–13553
- Merkel S, Hilairet N (2015) Multifit/Polydefix: a framework for the analysis of polycrystal deformation using X-rays. *J Appl Cryst* 48:1307–1313
- Miyazaki T, Sueyoshi K, Hiraga T (2013) Olivine crystals align during diffusion creep of Earth's upper mantle. *Nature* 502:321–326
- Nishihara Y, Ohuchi T, Kawazoe T, Spengler D, Tasaka M, Kikegawa T, Suzuki AM, Ohtani E (2014) Rheology of fine-grained forsterite aggregate at deep upper mantle conditions. *J Geophys Res Solid Earth* 119:253–273
- Ohuchi T, Irifune T (2014) Crystallographic preferred orientation of olivine in the Earth's deep upper mantle. *Phys Earth Planet Inter* 228:220–231
- Ohuchi T, Kawazoe T, Nishihara Y, Nishiyama N, Irifune T (2011) High pressure and temperature fabric transitions in olivine and variations in upper mantle seismic anisotropy. *Earth Planet Sci Lett* 304:55–63
- Paterson MS (1982) The determination of hydroxyl by infrared absorption in quartz, silicate glasses and similar materials. *Bull Minéral* 105:20–29
- Ponte Castañeda P (2002) Second-order homogenization estimates for nonlinear composites incorporating field fluctuations. i—theory. *J Mech Phys Solids* 50:737–757
- Raterron P, Chen J, Li L, Weidner D, Cordier P (2007) Pressure-induced slip-system transition in forsterite: single-crystal rheological properties at mantle pressure and temperature. *Am Mineral* 92:1436–1445
- Raterron P, Amiguet E, Chen J, Li L, Cordier P (2009) Experimental deformation of olivine single crystals at mantle pressures and temperatures. *Phys Earth Planet Inter* 172:74–83
- Raterron P, Chen J, Geenen T, Girard J (2011) Pressure effect on forsterite dislocation slip systems: implications for upper-mantle LPO and low viscosity zone. *Phys Earth Planet Inter* 188:26–36
- Raterron P, Girard J, Chen J (2012) Activities of olivine slip systems in the upper mantle. *Phys Earth Planet Inter* 200–201:105–112
- Takei H, Kobayashi T (1974) Growth and properties of Mg_2SiO_4 single crystals. *J Crystal Growth* 23:121–124
- Tommasi A, Mainprice D, Canova GR, Chastel Y (2000) Viscoplastic self-consistent and equilibrium-based modeling of olivine lattice preferred orientations: implications for the upper mantle seismic anisotropy. *J Geophys Res* 105:7893–7908
- Vaughan M, Chen J, Li L, Weidner D, Li B (2000) Of X-ray imaging techniques at high-pressure and temperature for strain measurements. In: Manghnani MH, Nellis WJ, Nicol MF (eds) *AIRAPT-17*. Universities Press, Hyderabad, pp 1097–1098
- Wang Y, Durham WB, Getting IC, Weidner DJ (2003) The deformation-DIA: a new apparatus for high temperature triaxial deformation to pressures up to 15 GPa. *Rev Sci Instrum* 74:3002
- Weidner DJ, Vaughan MT, Wang L, Long H, Li L, Dixon NA, Durham WB (2010) Precise stress measurements with white synchrotron X rays. *Rev Sci Instrum* 81:013903
- Wenk H-R, Matthies S, Donovan J, Chateigner D (1998) BEARTEX: a Windows-based program system for quantitative LPO analysis. *J Appl Cryst* 31:262–269
- Yuan K, Beghein C (2013) Seismic anisotropy changes across upper mantle phase transitions. *Earth Planet Sci Lett* 374:132–144